AGU PUBLICATIONS

JGR

Journal of Geophysical Research: Oceans

RESEARCH ARTICLE

10.1002/2015JC011183

Special Section:
Forum for Arctic Modeling and Observing Synthesis (FAMOS): Results and Synthesis of Coordinated Experiments

Ecosystem model intercomparison of under-ice and total primary production in the Arctic Ocean

Meibing Jin[1,2], Ekaterina E. Popova[3], Jinlun Zhang[4], Rubao Ji[5], Daniel Pendleton[6], Øystein Varpe[7,8], Andrew Yool[3], and Younjoo J. Lee[9]

[1]International Arctic Research Center, University of Alaska, Fairbanks, Alaska, USA, [2]Laboratory for Regional Oceanography and Numerical Modeling, Qingdao National Laboratory for Marine Science and Technology, Qingdao, China, [3]National Oceanography Centre, University of Southampton Waterfront Campus, Southampton, UK, [4]Polar Science Center, University of Washington, Seattle, Washington, USA, [5]Woods Hole Oceanographic Institution, Woods Hole, Massachusetts, USA, [6]New England Aquarium, Central Wharf, Boston, USA, [7]University Centre in Svalbard, Longyearbyen, Norway, [8]Akvaplan-niva, Fram Centre, Tromsø, Norway, [9]Bigelow Laboratory for Ocean Sciences, East Boothbay, Maine, USA

Abstract Previous observational studies have found increasing primary production (PP) in response to declining sea ice cover in the Arctic Ocean. In this study, under-ice PP was assessed based on three coupled ice-ocean-ecosystem models participating in the Forum for Arctic Modeling and Observational Synthesis (FAMOS) project. All models showed good agreement with under-ice measurements of surface chlorophyll-a concentration and vertically integrated PP rates during the main under-ice production period, from mid-May to September. Further, modeled 30-year (1980–2009) mean values and spatial patterns of sea ice concentration compared well with remote sensing data. Under-ice PP was higher in the Arctic shelf seas than in the Arctic Basin, but ratios of under-ice PP over total PP were spatially correlated with annual mean sea ice concentration, with higher ratios in higher ice concentration regions. Decreases in sea ice from 1980 to 2009 were correlated significantly with increases in total PP and decreases in the under-ice PP/total PP ratio for most of the Arctic, but nonsignificantly related to under-ice PP, especially in marginal ice zones. Total PP within the Arctic Circle increased at an annual rate of between 3.2 and 8.0 Tg C/yr from 1980 to 2009. This increase in total PP was due mainly to a PP increase in open water, including increases in both open water area and PP rate per unit area, and therefore much stronger than the changes in under-ice PP. All models suggested that, on a pan-Arctic scale, the fraction of under-ice PP declined with declining sea ice cover over the last three decades.

Key Points:
- Total primary production within the Arctic Circle increased 3.2–8 Tg C/yr
- Fraction of under-ice production declined with declining sea ice cover over in Arctic
- Increase in total production was due to increased open water areas and production rate

Correspondence to:
M. Jin,
mjin@alaska.edu

Citation:
Jin, M., E. E. Popova, J. Zhang, R. Ji, D. Pendleton, Ø. Varpe, A. Yool, and Y. J. Lee (2016), Ecosystem model intercomparison of under-ice and total primary production in the Arctic Ocean, *J. Geophys. Res. Oceans*, *121*, 934–948, doi:10.1002/2015JC011183.

Received 28 JUL 2015
Accepted 21 DEC 2015
Accepted article online 28 DEC 2015
Published online 27 JAN 2016

1. Introduction

The decline of sea ice cover in the Arctic Ocean is an iconic feature of global warming. Meanwhile, Arctic Ocean primary production (PP) has been increasing due to increased open water and light availability, as revealed by remote sensing data [*Pabi et al*., 2008; *Arrigo and van Dijken*, 2011]. The PP underneath sea ice was not included in remote sensing and most ship-based observations, and previously thought to be small, but recently found to be significant in the Chukchi Sea [*Arrigo et al*., 2012].

Ecosystem models are useful tools for filling the large gaps between remote sensing in the open water and sparse in situ observations in sea ice covered areas. A previous Arctic ecosystem model intercomparison study [*Popova et al*., 2012] found that models produced broadly similar sea ice conditions and annual vertically integrated PP, though nutrients were different between models due to different magnitudes of vertical mixing. Because Arctic PP was colimited by nutrients and light, similar PP in different models may be produced due to different limiting factors in different models. The intercomparison in *Popova et al*. [2012] focused on the controlling factors of Arctic oceanic PP, and did not differentiate between PP under ice or in open water.

The ecosystem model of *Zhang et al*. [2015] simulated the under-ice blooms observed in the Chukchi Sea by *Arrigo et al*. [2012], and confirmed the existence of under-ice production even before the recent, dramatic Arctic warming. That model was only compared with observations in the Chukchi Sea [*Arrigo et al*., 2012], however, and did not examine under-ice PP on a pan-Arctic scale. The focus of the ecosystem model

Table 1. Comparison of Physical and Ecosystem Model Configuration

	NEMO	UW	LANL-UAF
Forcing	Coupled model output (HadGEM2-ES) [*Jones et al.*, 2011]	6 hourly NCEP/NCAR reanalysis	6 hourly NCEP/NCAR reanalysis data
Simulation period	1860–2099	1971–present	1958–2009
Model domain	Global	North of 39°N	Global
Horizontal andvertical resolution	0.25°, approximately 30 km 75 layers, 1 m at surface	2 to ~100 km 30 layers, 5 m at surface	30–50 km in the Arctic 40 layers, 10 m at surface
Nutrients	NO_3, SiO_3, and Fe	NO_3, NH_4, and SiO_3	NO_3, NH_4, SiO_3, Fe, and PO_4
Phytoplankton	Diatoms (microphytoplankton) and nondiatoms (nanophytoplankton)	Diatom and flagellates	Diatom, flagellates, and diazotroph
Sea ice algae	No ice algae	In ice bottom 2 cm	In ice bottom 3 cm

intercomparison study here is to understand how well ecosystem models are able to capture historically available observations of under-ice PP over the pan-Arctic Ocean. The long time series of under-ice and total PP (sum of PP under ice and in open water) from participating ecosystem models could contribute to assessing potential impacts of climate changes on pelagic and benthic ecosystems, especially in shallow shelf regions. However, ice algae, which grow inside the ice column, are not assessed in this study, as not all models include this component.

2. Participating Models

The three models participating in this study have been used similarly in a previous intercomparison study regarding controls for Arctic PP [*Popova et al.*, 2012]. For this study, we did not set protocols for input forcing, but output variables were saved in 5 day interval and spatially interpolated onto a uniform grid (1° in longitude and 0.4° in latitude) to the north of 66.5°N. Main differences between participating models are summarized in Table 1, with further details for each model, including recent updates, described in the following sections.

2.1. NEMO

The physical framework used here is the Nucleus for European Modelling of the Ocean (NEMO) model [*Madec*, 2008], composed of the ocean general circulation model (GCM) Ocean PArallelise version 9 (OPA9) [*Madec et al.*, 1998; *Madec*, 2008] coupled to the sea ice submodel Louvain-la-Neuve Ice Model version 2 (LIM2) [*Timmermann et al.*, 2005].

OPA9 is a primitive equation GCM, configured here at a horizontal resolution of approximately 0.25° (1442 × 1021 grid cells). The vertical space is divided into 75 levels, which increase in thickness with depth, from 1 m at the surface to 200 m at 6000 m. To better represent bottom topography and deep circulation, OPA9 includes partial level thickness cells at the seafloor. The turbulent kinetic energy (TKE) scheme [*Gaspar et al.*, 1990; *Madec*, 2008] is used for calculating vertical mixing.

LIM2 is based on viscous-plastic ice rheology [*Hibler*, 1979] with three layer (two × ice, one × snow) thermodynamics [*Semtner*, 1976; *Timmermann et al.*, 2005]. NEMO's sea ice model couples to the ocean model every five ocean time steps through a nonlinear quadratic drag law of the velocity shear between ocean and sea ice [*Timmermann et al.*, 2005]. Freshwater exchange is calculated from ice formation/melting and precipitation, while heat flux is proportional to the friction velocity at the ice-ocean interface and the temperature departure from the salinity-dependent freezing point.

The biogeochemistry component used here is the Model of Ecosystem Dynamics, nutrient Utilisation, Sequestration, and Acidification (MEDUSA-2) [*Yool et al.*, 2013a]. This is a so-called "intermediate complexity" model of the plankton ecosystem, founded on the oceanic nitrogen cycle. Though simplified, MEDUSA-2 is designed to retain sufficient complexity to tackle primary feedbacks between ocean biogeochemical cycles and anthropogenic drivers such as climate change and ocean acidification. The model includes elemental cycles of carbon (and alkalinity), nitrogen, silicon, iron, and oxygen, all linked in a dual size-class Nutrient-Phytoplankton-Zooplankton-Detritus (NPZD) model. The modeled tracers include dissolved nitrogen, silicon, and iron nutrients; "small" (nanophytoplankton and microzooplankton) and "large" (microphytoplankton and mesozooplankton)

living components; and two pools of sinking detrital material. "Large" phytoplankton are assumed to be synonymous with diatoms in MEDUSA-2, and have a corresponding requirement for silicon [*Mongin et al*., 2006]. "Small" detritus is assumed to be slow-sinking and is modeled explicitly, while "large" detritus is assumed to be fast-sinking and is modeled implicitly, using a variant of the *Armstrong et al*. [2002] ballast model [*Klaas and Archer*, 2002; *Dunne et al*., 2007]. Here the ballast model is framed using biogenic fluxes of opal [*Mongin et al*., 2006] and calcium carbonate [*Ridgwell et al*., 2007].

Simulations using a "medium resolution" instance of NEMO and MEDUSA-2 have been published previously by *Yool et al*. [2013b] and *Popova et al*. [2014]. This model has also been used in several model intercomparison studies [i.e., *Popova et al*., 2012; *Kwiatkowski et al*., 2014].

2.2. UW Model

The UW model is the *B*iology/*I*ce/*O*cean *M*odeling and *A*ssimilation *S*ystem (*BIOMAS*), a coupled biophysical model [*Zhang et al*., 2010a,] with four model elements: a sea ice model, an ocean circulation model, a pelagic biological model, and a sea ice algae model. The pelagic biological model is an 11-component marine pelagic ecosystem model, including two phytoplankton components (diatoms and flagellates), three zooplankton components (microzooplankton, copepods, and predatory zooplankton), dissolved organic nitrogen, detrital particulate organic nitrogen, particulate organic silica, nitrate, ammonium, and silicate [see *Zhang et al*., 2014, Figure 3; also see *Kishi et al*., 2007]. Values for key biological parameters used in the model are listed in *Zhang et al*. [2010a].

The sea ice algal component of BIOMAS represents colonies in a 2 cm layer at the bottom of each of eight sea ice thickness categories, coupled to the pelagic model through nutrient and biotic fluxes. The sea ice algae model has two ice algae components (diatoms and flagellates), with nitrate, ammonium, and silicate as limiting nutrients for ice algal growth. Nutrient and biotic exchange at the ice and water interface is based on *Jin et al*. [2006]. Simulated ice algal production and biomass have been validated using observations of the Shelf-Basin Interaction Program (SBI), collected from the shelves and slope regions of the Chukchi and Beaufort seas [*Gradinger*, 2009].

The ocean circulation model is based on the Parallel Ocean Program (POP), developed at Los Alamos National Laboratory [*Smith et al*., 1992] and modified by *Zhang and Steele* [2007] so that open boundary conditions can be specified. The POP ocean model is further modified by *Zhang et al*. [2010b] to incorporate tidal forcing from eight primary constituents [*Gill*, 1982]. This forcing consists of a tide-generating potential with corrections for both the earth tide and self-attraction and loading, following *Marchuk and Kagan* [1989].

The sea ice model is a thickness and enthalpy distribution (TED) sea ice model [*Zhang and Rothrock*, 2003; *Hibler*, 1980], with eight categories each for ice thickness, ice enthalpy, and snow depth. It is adopted from the *P*an-arctic *I*ce/*O*cean *M*odeling and *A*ssimilation *S*ystem (PIOMAS) [*Zhang and Rothrock*, 2003] and capable of assimilating satellite observations of sea ice concentration [*Lindsay and Zhang*, 2006] and sea surface temperature [*Manda et al*., 2005; *Schweiger et al*., 2011]. More BIOMAS details, including model configuration, forcing, and initial conditions, are given in *Zhang et al*. [2015]. Values of ice algae concentration are initialized as zero in the sea ice algae model.

2.3. LANL-UAF

A marine biogeochemical (mBGC) module [*Moore et al*., 2004; *Jin et al*., 2012] is incorporated in a global version of the POP-CICE (Parallel Ocean Program—Sea ICE) model developed at Los Alamos National Laboratory (LANL). In this study, the model uses a 320 $\times$ 384 global mesh with the "north pole" of the model grid moved to Greenland, to avoid grid singularity at the geographical North Pole. The Northern Hemisphere grid size ranges from 18 km (at high latitudes) to 85 km (at the equator). The vertical grid consists of 40 levels, varying in thickness from 10 m at the surface to 250 m below 2000 m depths. Atmospheric forcing data include 6 hourly air temperature, specific humidity, and wind velocity components from the Common Ocean Reference Experiments (CORE) version 2 [*Large and Yeager*, 2009]. These data, along with version 2 of the Ocean Model Intercomparison Project's cloud climatology [*Röske*, 2001], are used to calculate radiation fields following the AOMIP protocol. Total runoff in the Arctic is also specified following the AOMIP protocol [*Hunke and Holland*, 2007]. The present model run covers 1958–2009. The ocean component, POP 2.0 [*Smith and Gent*, 2002], employs the anisotropic Gent-McWilliams parameterization of *Smith and Gent* [2004] for lateral mixing. The K-profile parameterization (KPP) [*Large et al*., 1994] provides vertical mixing of

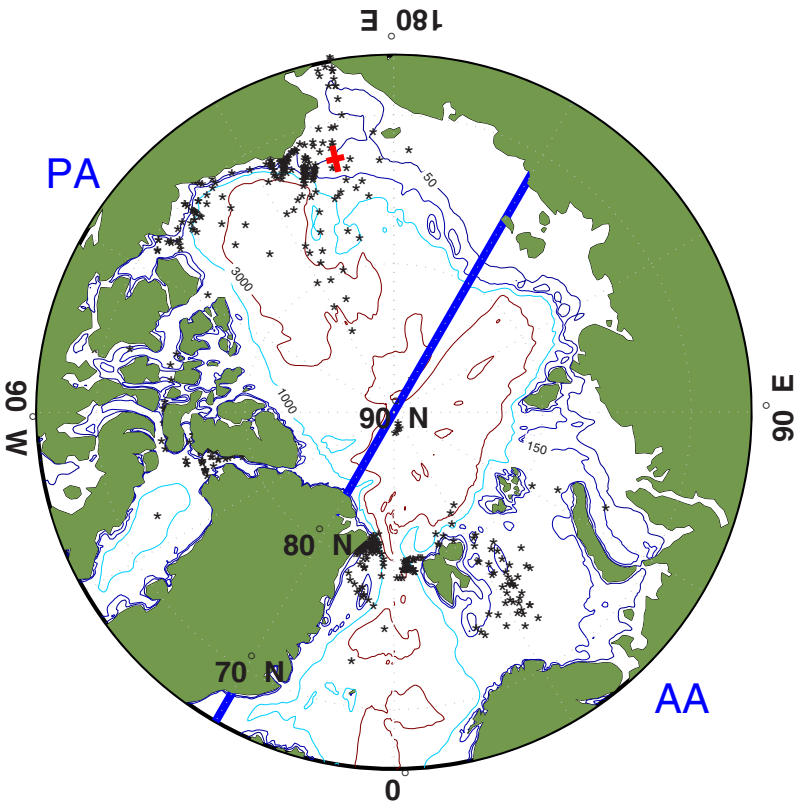

Figure 1. Map of the Arctic Ocean. Contour lines denote depths at 50, 150, 1000, and 3000 m. Red cross denotes point A (167°W, 72.4°N). Black "*" denotes in situ data points with under-ice measurements. The Arctic Ocean is divided by the blue line into the Pacific Arctic (PA) and the Atlantic Arctic (AA), for model validation.

momentum and tracers. The sea ice component, CICE [*Hunke et al*., 2013], includes *Bitz and Lipscomb* [1999] thermodynamics, elastic-viscous-plastic (EVP) dynamics [*Hunke and Dukowicz*, 1997], and horizontal transport via incremental remapping [*Lipscomb and Hunke*, 2004]. The thickness distribution within each grid cell is represented using five thickness categories, each with a single layer of snow atop four layers of ice.

After the last ecosystem model comparison led by *Popova et al*. [2012], this model has been implemented with a subgrid-scale ocean mixing scheme for under-sea ice ocean mixing [*Jin et al*., 2012], which greatly reduced model errors in simulated mixed layer depth, salinity, and nutrients in the Arctic Ocean.

The pelagic component of mBGC is a medium-complexity NPZD model, derived from *Moore et al*. [2002, 2004]. The model includes 26 state variables: nitrate (NO_3), ammonium (NH_4), phosphate (PO_4), silicate (Si), iron (Fe), three types of phytoplankton (diatoms, small phytoplankton (flagellates), and diazotrophs, with explicit carbon, Fe, and chlorophyll-a concentration (Chl-a) pools for each phytoplankton group, an explicit Si pool for diatoms, and an implicit calcium carbonate ($CaCO_3$) pool for small phytoplankton, totaling 11 state variables), a herbivorous zooplankton pool, dissolved organic carbon (DOC), nitrogen (DON), iron (DOFe), and phosphorus (DOP), oxygen, dissolved inorganic carbon (DIC), alkalinity, dimethyl sulfide (DMS), and dimethylsulfoniopropionate (DMSP).

The ice algal component of mBGC represents colonies in a 3 cm layer at the bottom of each sea ice thickness category, coupled to the pelagic model through nutrient and biotic fluxes. Initial development of this submodel was based on biophysical ice core data collected in land-fast ice offshore from Barrow, Alaska [*Jin et al*., 2006]. The ice algal model was later applied and further developed in coupling with a pelagic ecosystem model in vertically 1-D models [*Jin et al*., 2007] and global POP-CICE model settings [*Deal et al*., 2011; *Jin et al*., 2012]. It includes six components: ice algae, NO_3, NH_4, Si, DMS, and DMSP. Initial conditions for chemical variables (NO_3 and Si) are from the gridded World Ocean Atlas [*WOA*, 2005], and for other constituents from a global model simulation by *Moore et al*. [2004].

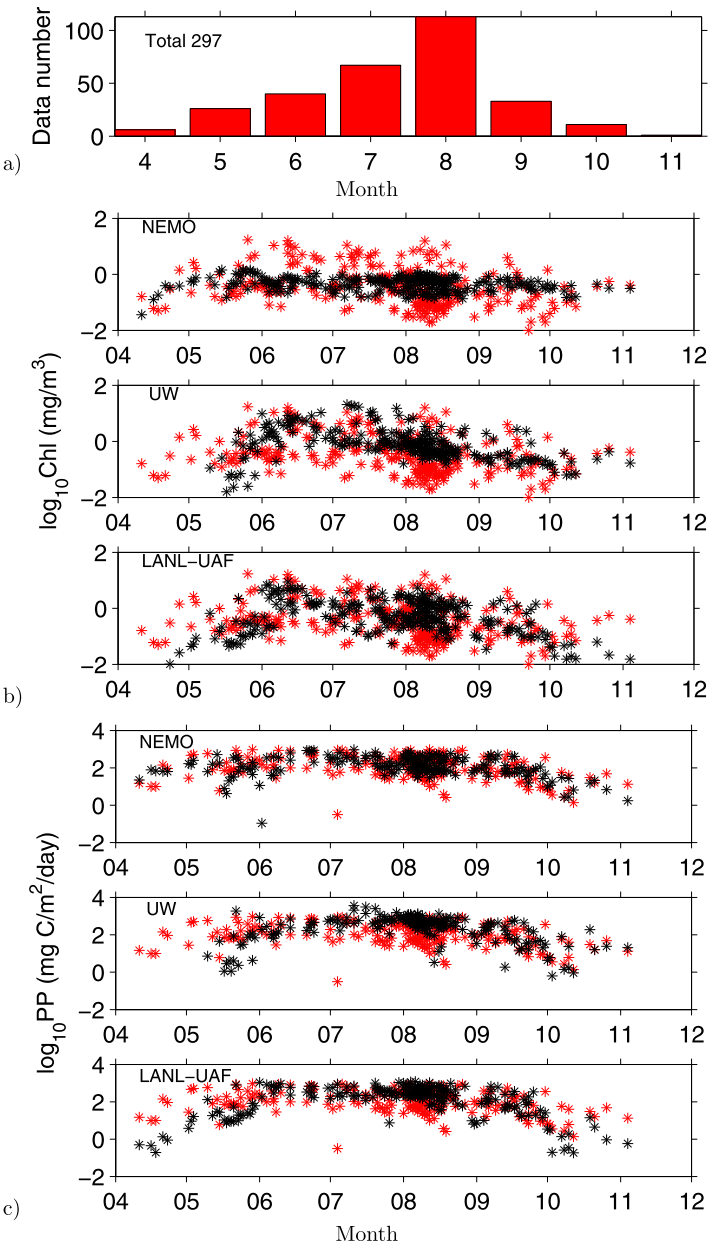

Figure 2. Model (black "*") validation with under-ice measurements (red "*") in the Pacific Arctic (150°E to 30°W); (a) monthly distribution of the number of in situ observations, (b) sea surface Chl-a, (c) vertically integrated PP rate.

3. Results

3.1. Model Comparison With Under-Ice Measurements

Since all models have been validated with remote sensing surface Chl-a and other in situ observations in open water [*Popova et al.*, 2012; *Zhang et al.*, 2010a, 2015; *Jin et al.*, 2012], this study focuses on validation with under-ice measurements of Chl-a and PP rate.

Matrai et al. [2013] synthesized available PP observations from 1954 to 2007, recently updating them to 2011 for the Arctic Ocean. Among these data, there are only 490 stations with under-ice measurements of surface Chl-a and vertically integrated PP available for the 1980–2009 model intercomparison period (Figure 1). Few data are available for the Canadian Archipelago and East Siberian Sea, and all data can be divided into two ecological regions: the Pacific Arctic (PA), from 150°E to 30°W, and the Atlantic Arctic (AA), from 30°W to 150°E. Data availability per region and calendar month are shown in Figures 2a and 3a. For comparison, model output was extracted from the same day and location as observations to calculate mean, standard deviation (SD), and root-mean-square error (RMSE) (Table 2).

Data in the PA were collected primarily in August and to a lesser extent in earlier and later months (Figure 2a). All models and data showed low Chl-a and PP rate in April and onset of blooms in May (Figure 2). Chl-a and PP rate in all models reached the same level as observations in late May and June, despite some discrepancies in April, with very low under-ice PP. All modeled Chl-a and PP rates were within the range of observations (Figures 2). The root-mean-square errors (RMSE) of modeled Chl-a and PP rates were in the ranges of 0.154–0.215 mg/m^3 and 17.4–37.0 mg C/m^2/d, respectively, and relative errors were within 12–17% and 8–17%, respectively (Table 2). The models did not capture the lower Chl-a and parts of the lower PP values in August. This is likely caused by overestimation of nutrients in the surface water due to models' inability to simulate the strong upper ocean stratification after ice melt. Means and SDs of modeled Chl-a and PP rates spread around observations with lower values in NEMO, higher values in UW, and mixed values in LANL-AUF (Table 2). Declines in PP rate from September to October were well simulated by all models (Figure 2).

Table 2. Mean, Standard Deviation (SD), Root-Mean-Square Error (RMSE), and Relative Errors (RMSE/In Situ Mean) of Modeled and Observed Surface Chl-a and Vertically Integrated PP Rates

			NEMO	UW	LANL-UAF	In Situ Data
Pacific Arctic region	Surface Chl-a (mg/m^3)	Mean	0.529	1.861	1.068	1.238
		SD	0.268	3.501	1.322	2.538
		RMSE	0.156	0.215	0.154	
		RMSE/(in situ mean)	13%	17%	12%	
	Vertically integrated PP rate ($mg\ C/m^2/d$)	Mean	206	422	293	216
		SD	195	488	280	233
		RMSE	17.4	37.0	22.8	
		RMSE/(in situ mean)	8%	17%	11%	
Atlantic Arctic region	Surface Chl-a (mg/m^3)	Mean	0.713	0.672	1.301	1.160
		SD	0.565	0.572	1.363	1.573
		RMSE	0.125	0.133	0.160	
		RMSE/(in situ mean)	11%	11%	14%	
	Vertically integrated PP rate ($mg\ C/m^2/d$)	Mean	340	226	460	420
		SD	291	203	438	258
		RMSE	35.8	36.6	49.3	
		RMSE/(in situ mean)	9%	9%	12%	

Fewer observations were available from the AA than the PA. In situ measurements in the AA were collected most frequently in July, less frequently in other months, and least frequently in September (Figure 3a). Under-ice bloom beginning and ending times in the AA were about half a month earlier than in the PA (Figures 3b and 3c, compared to Figures 2b and 2c). Observations showed that Chl-a and PP rate began to increase in early April, reaching summer levels later in the month. All modeled Chl-a and PP rates from mid-May to September matched with the observational mean and their range of variations, but model biases were higher at stations with the lowest and highest values than at stations with average values. The RMSE of modeled Chl-a and PP rates were in the ranges of 0.125–0.160 mg/m^3 and 35.8–49.3 $mg\ C/m^2/d$, respectively, and relative errors were within 11–14% and 9–12% (Table 2). In contrast to the PA, the UW model showed lower mean and SD than did observations in the AA, while NEMO showed lower values (except for a higher SD for PP rate) and LANL-UAF showed higher values (except for a lower SD for Chl-a).

Overall, most model simulation of under-ice Chl-a and PP rates was within ranges of observations for the main bloom period from mid-May to September, though some discrepancies existed in April before under-ice blooms start. Modeled means and SDs from the three models showed both higher and lower values than observations, without systematic bias.

3.2. Sea Ice Conditions and Under-Ice Production

The 30 (1980–2009) average for modeled sea ice concentration was compared with National Snow and Ice Data Center (NSIDC) Special Sensor Microwave Imager (SSM/I) data for the same period (Figure 4). All models captured spatial patterns of observed ice concentration, except in small areas of the Arctic Basin (Figure 4). The under-ice PP averaged from 1980 to 2009 was higher in Arctic Shelf seas than in the Arctic Basin for all models (Figures 5a–5c), but ratios of under-ice PP over total PP (Figures 5d–5f) resembled sea ice concentration (Figure 4), with higher than 90% ratios where average ice concentration was larger than 80%. Ratios were generally lower in seasonally ice-covered seas, with a lower annual average ice concentration.

Pearson correlation coefficient r values (scaled from 0 to 1) and p values (correlation is statistically significant if $p < 0.05$) between sea ice concentration and total PP, under-ice PP, and corresponding ratios are shown in Figures 6–8, respectively. Correlations with total PP were significant and negative due to increasing light through ice or an increasing open water period, except for small regions in the Arctic Basin in the UW model (Figure 6). Sea ice concentration showed no significant correlation with under-ice PP in marginal ice zones for all models (Figure 7), as under-ice PP is affected by two contradicting trends: an increase due to increasing light through ice and a decrease due to decreasing ice-covered time. The correlation between ice concentration and under-ice PP was mostly significant and negative in the Arctic Basin for NEMO and LANL-UAF, but nonsignificant in part of the Arctic Basin for UW, likely because PP was limited by nutrient depletion rather than light in these areas. Because total PP increased at a much higher rate than that of under-ice PP, correlations between ice concentration and the ratios of under-ice PP/total PP were significant and positive in most regions for all models (Figure 8).

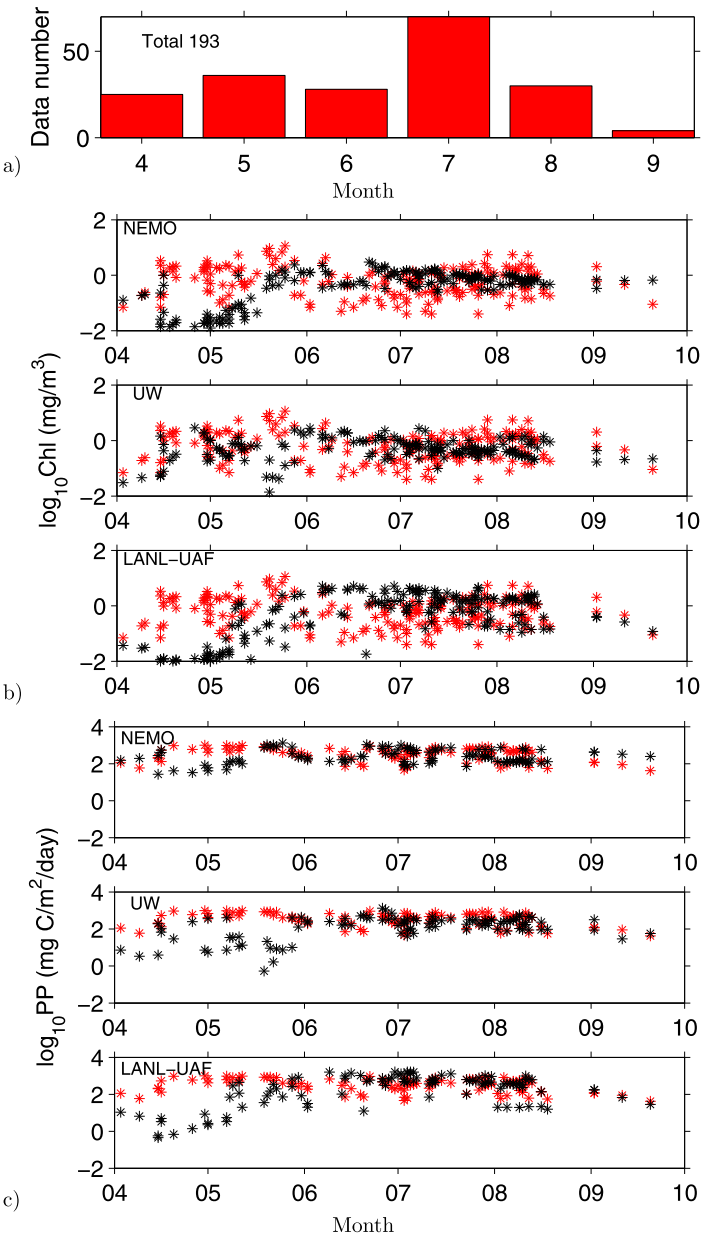

Figure 3. Model (black "*") validation with under-ice measurements (red "*") in the Atlantic Arctic (30°W to 150°E); (a) monthly distribution of the number of in situ observations, (b) sea surface Chl-a, (c) vertically integrated PP rate.

The modeled sum of PP within the Arctic Circle (Figures 9a–9c) showed strong consensus on an increasing trend from 1980 to 2009, at a rate between 3.2 and 8.0 Tg C/yr, while models differed on the trends of under-ice PP, with one decreasing and two increasing trends (−0.9, 0.2, and 0.9 Tg C/yr). This is because under-ice PP was determined by two contradictory factors (Figure 10): declining ice covered area and increasing light availability, coinciding with a general warming trend in the Arctic. Total PP, meanwhile, was determined by four factors, with the negative (decreasing trend) factor offset by one of the three positive (increasing trend) ones: decreasing ice covered area was offset by increasing open water area. PP per unit area (Figures 9d–9f) increased at rates of 0.04–0.17 g C/m^2/yr in open water, but changed at a much weaker trend of −0.0028 to 0.0029 g C/m^2/yr under ice. UW is the only model showing decreasing trends for total and per unit area of under-ice PP, likely because of greater sea ice loss in highly productive areas and stronger nutrient limitation in the Arctic Basin in UW than in other models.

To summarize findings from Figures 6 to 9: the increase in total PP was much greater than the changes in under-ice PP, and therefore under-ice pp/total PP ratios decreased during the last 30 years for all model simulations. The total PP increase was due mainly to a PP increase in open water, including increases in both open water area and PP rate per unit area.

3.3. Controlling Factors for Under-Ice Production

In order to understand controlling factors for under-ice PP in different models, the model time series at point A (Figure 1), which is on the cruise section where *Arrigo et al.* [2012] found a massive under-ice bloom in July 2011, were extracted for comparison. Figure 11 showed seasonal (mid-May to mid-November) and interannual variations in modeled ice thickness and shortwave radiation at the sea surface (or at the ice bottom). All models showed decreasing ice thickness and earlier ice melt over the last 30 years, though they differed in magnitude. Light availability (Figure 11) also trended earlier for all models, triggering earlier phytoplankton blooms. This is mainly because the early stage for blooms was predominantly light-limited.

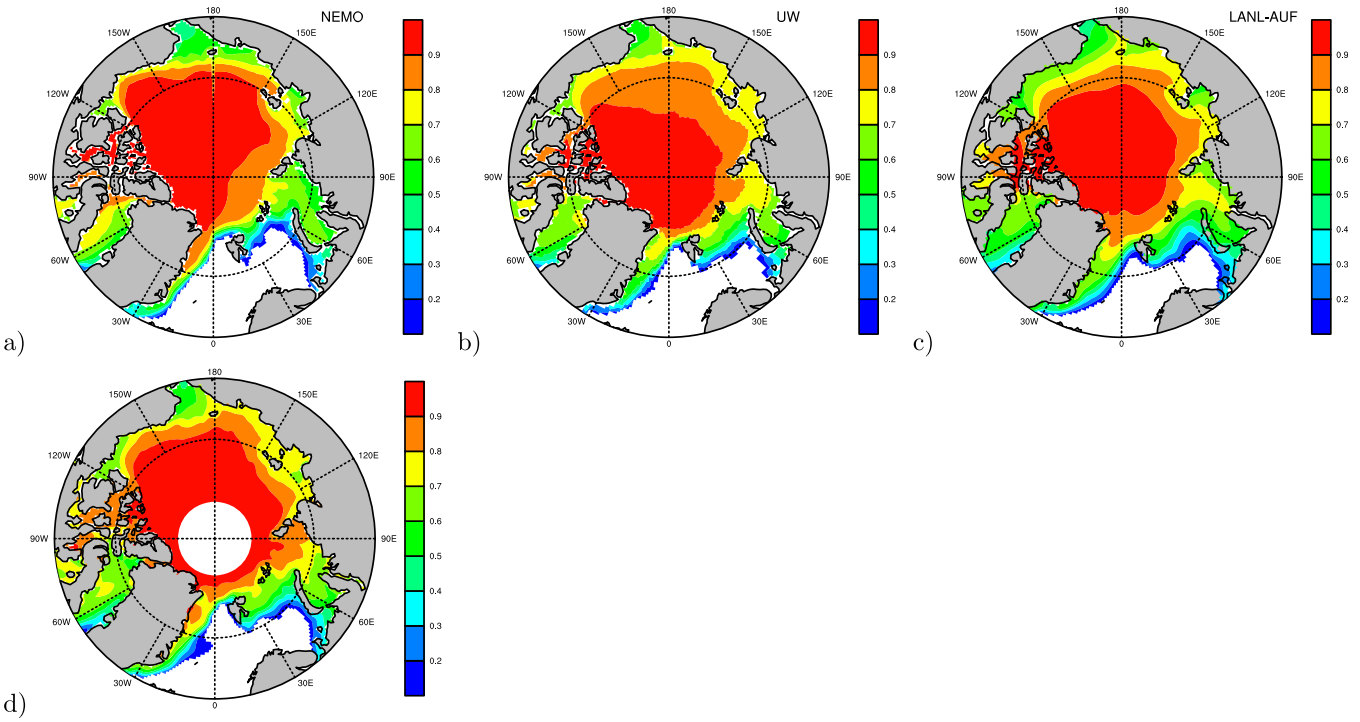

Figure 4. Annual mean climatology (1980–2009) of sea ice concentration from (a) NEMO, (b) UW, (c) LANL-UAF, and (d) NSIDC data.

Modeled light was highest in UW and lowest in NEMO. Consequently, under-ice Chl-a blooming was strongest in UW and weakest in NEMO, while nitrate consumption was highest in UW and lowest in NEMO (Figure 12). For July to August, nitrate was mostly depleted and PP was strongly nutrient-limited in UW; nitrate was not depleted in any years for NEMO or during the 1980s for LANL-UAF, though it was depleted after 1995 for LANL-UAF. Prebloom (before June) nitrate and PP rate in NEMO was lower than the other two models.

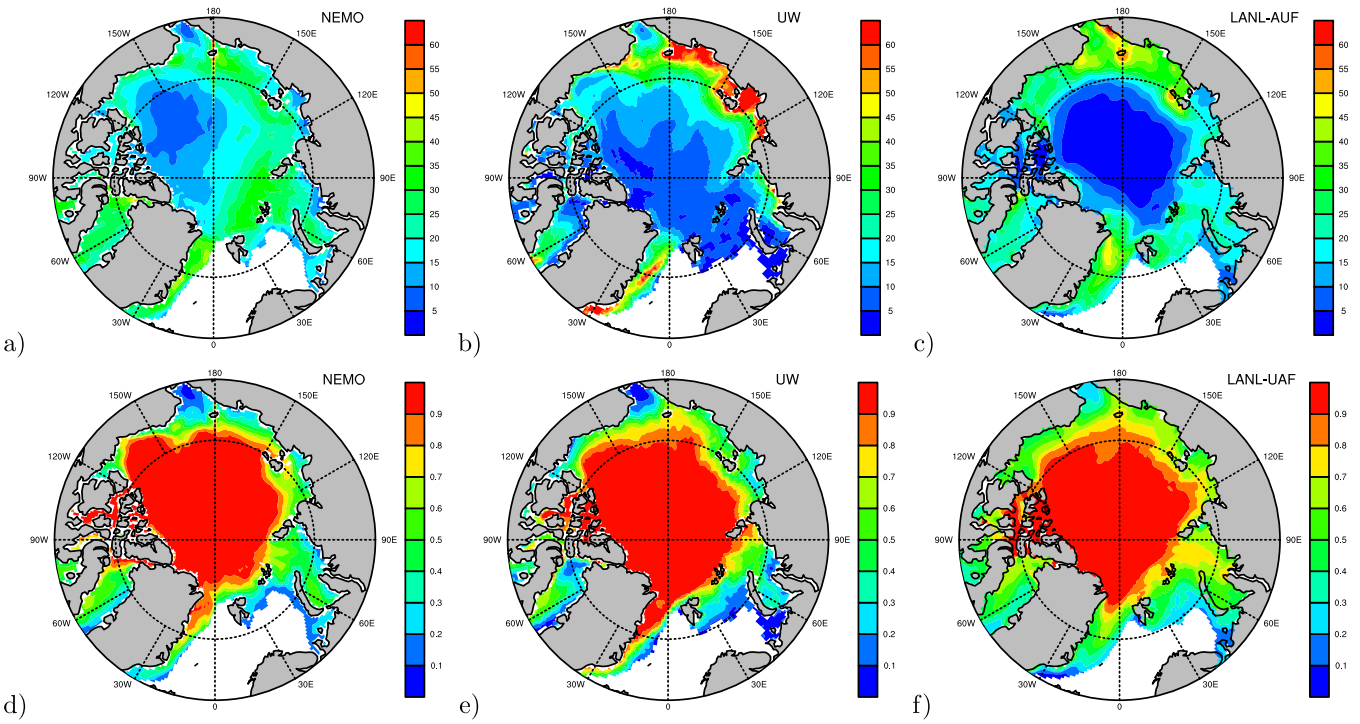

Figure 5. Annual mean (1980–2009) of under-ice PP from (a) NEMO, (b) UW, and (c) LANL-AUF; and average ratio of under-ice PP over total PP from (d) NEMO, (e) UW, and (f) LANL-AUF.

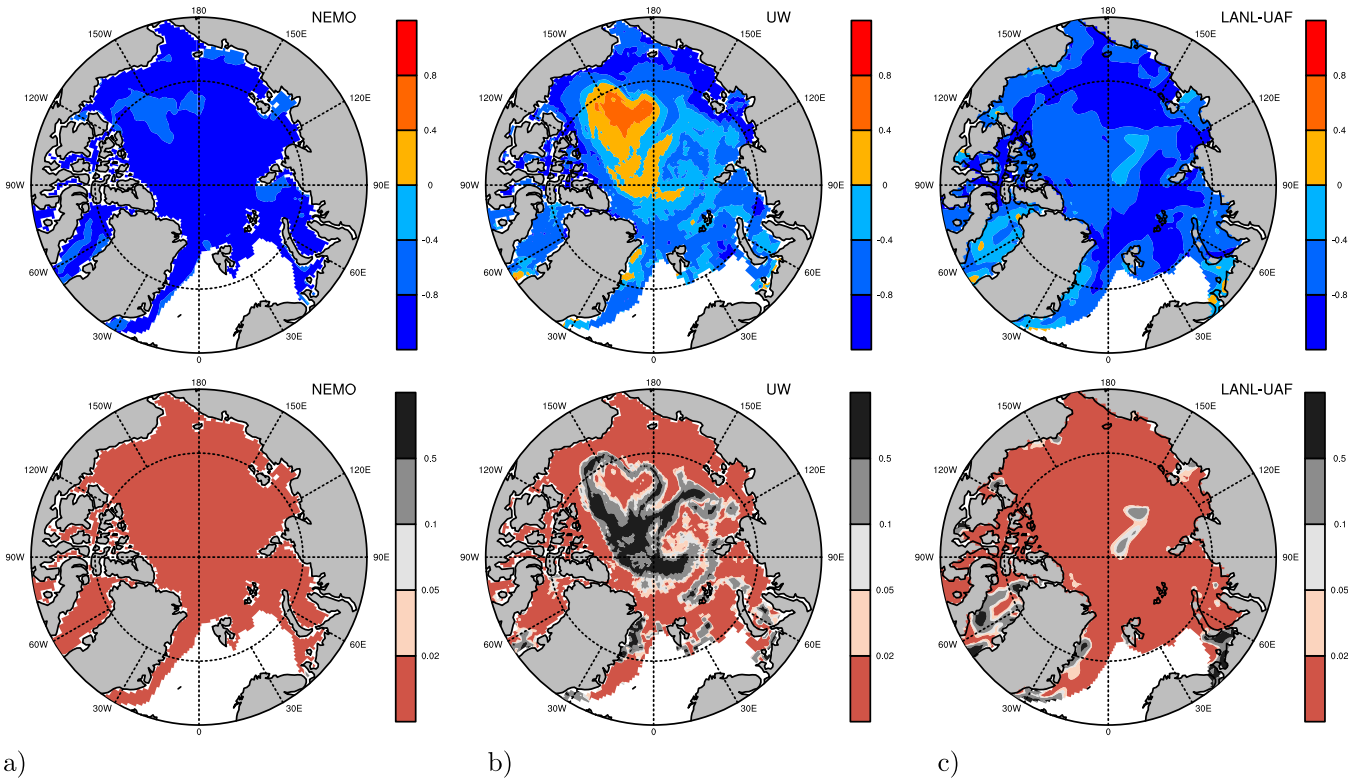

Figure 6. (top row) *r* Value and (bottom row) *p* value of Pearson's correlations between sea ice concentration and total PP from 1980 to 2009 from (a) NEMO, (b) UW, and (c) LANL-AUF.

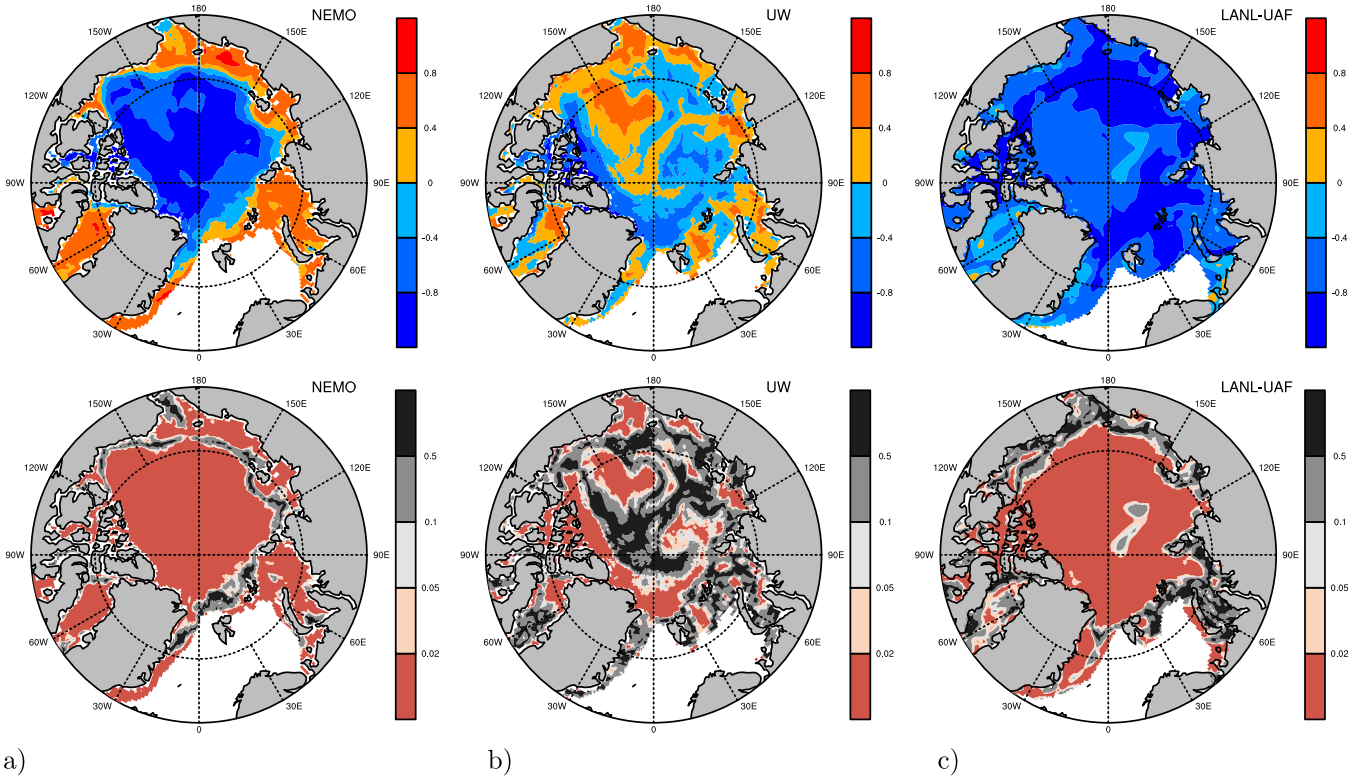

Figure 7. Same as Figure 6, with under-ice PP instead of total PP.

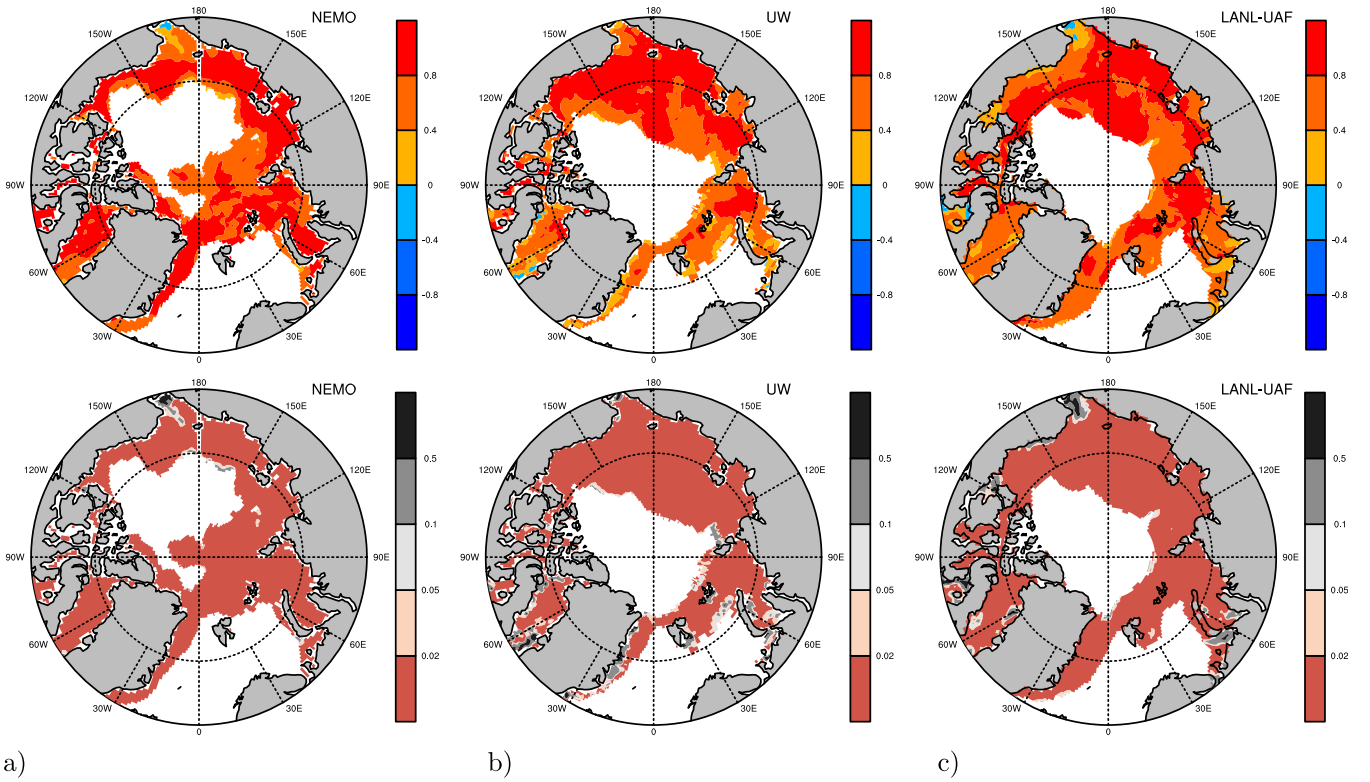

Figure 8. (top row) *r* Value and (bottom row) *p* value (lower row) of Pearson's correlations between sea ice concentration and the ratio of under-ice over total PP from 1980 to 2009 from (a) NEMO, (b) UW, and (c) LANL-AUF. White areas denote areas either with no sea ice or always covered by sea ice, such as in the central Arctic, where the ratio is always 1.

Since nitrate was not depleted in NEMO, the limiting effect of light on the PP rate in NEMO was relatively higher. The difference in light intensity between models was most likely caused by different sources of atmospheric forcing in the models. Atmospheric forcing was from the atmospheric model in a fully coupled climate model, while UW and LANL-UAF used NCEP reanalysis products (Table 1), which have been adjusted

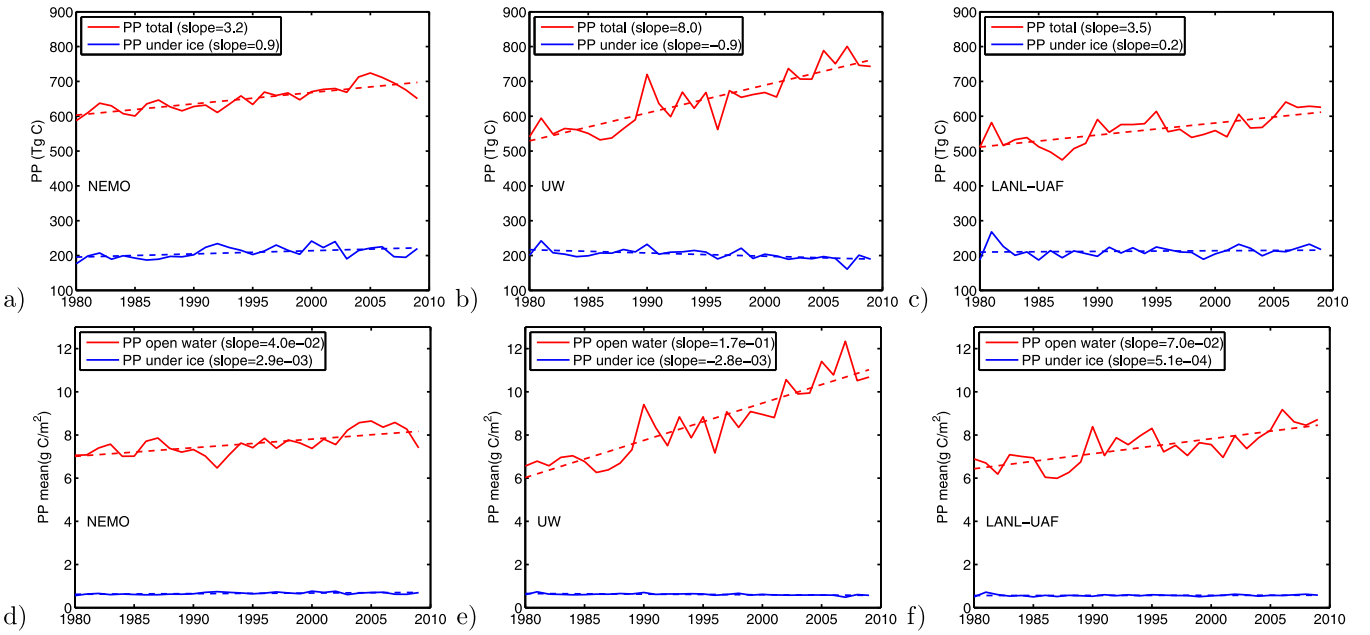

Figure 9. Time series of total PP and under-ice PP within the Arctic Circle; daily sum from (a) NEMO, (b) UW, and (c) LANL-UAF; PP per unit area in open water and under-ice-covered regions from (d) NEMO, (e) UW, and (f) LANL-UAF. Dashed lines denote a linear regression fit.

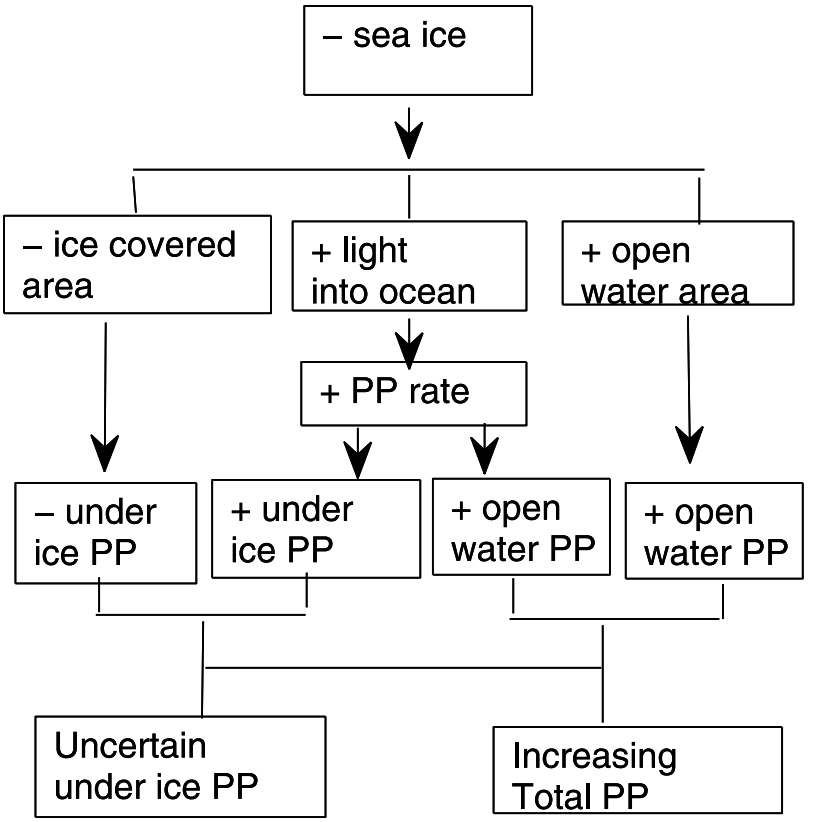

Figure 10. Schematic chart of factors affecting total and under-ice PP associated with the declining sea ice cover trend. Symbols "+" and "−" denote increasing and decreasing trends, respectively.

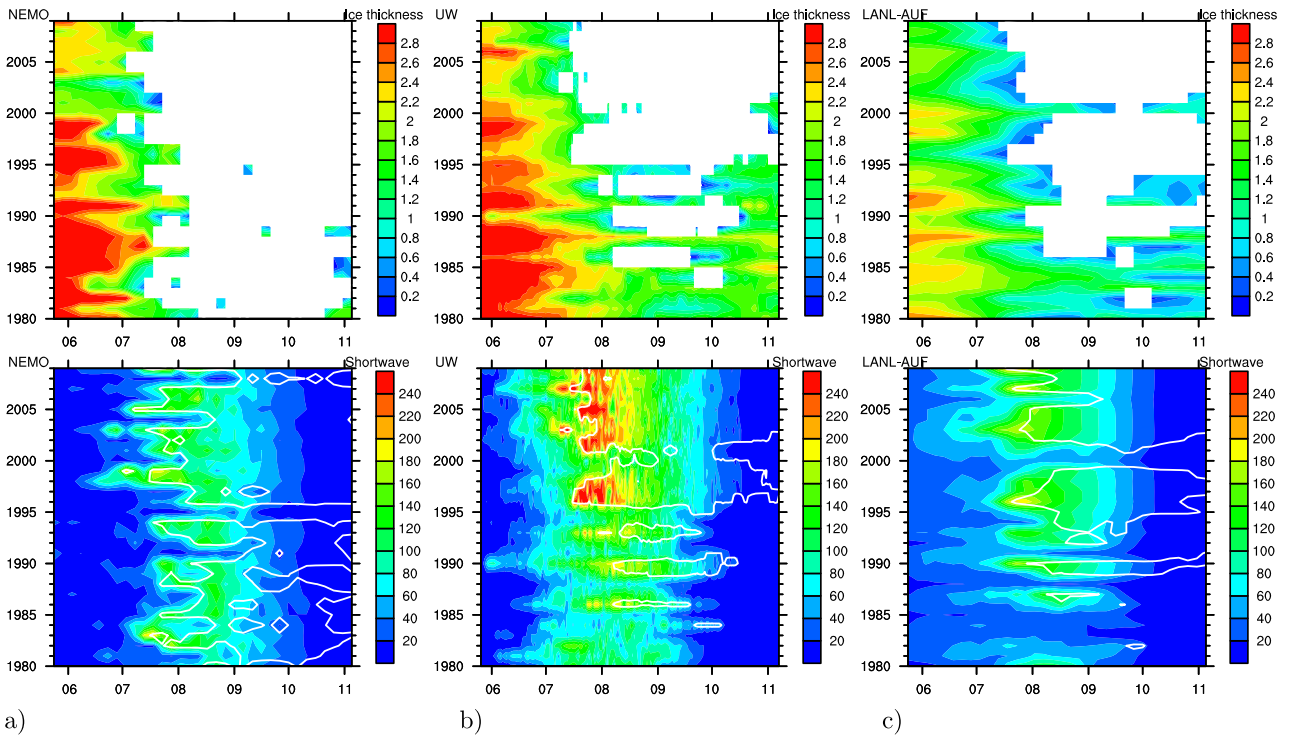

Figure 11. (top row) Seasonal and interannual variation in ice thickness (m) and (bottom row) shortwave radiation (W/m^2) at point A (1980–2009) from (a) NEMO, (b) UW, and (c) LANL-UAF. White contour lines denote the 15% ice concentration. The *x* axis denotes month, and *y* axis denotes year.

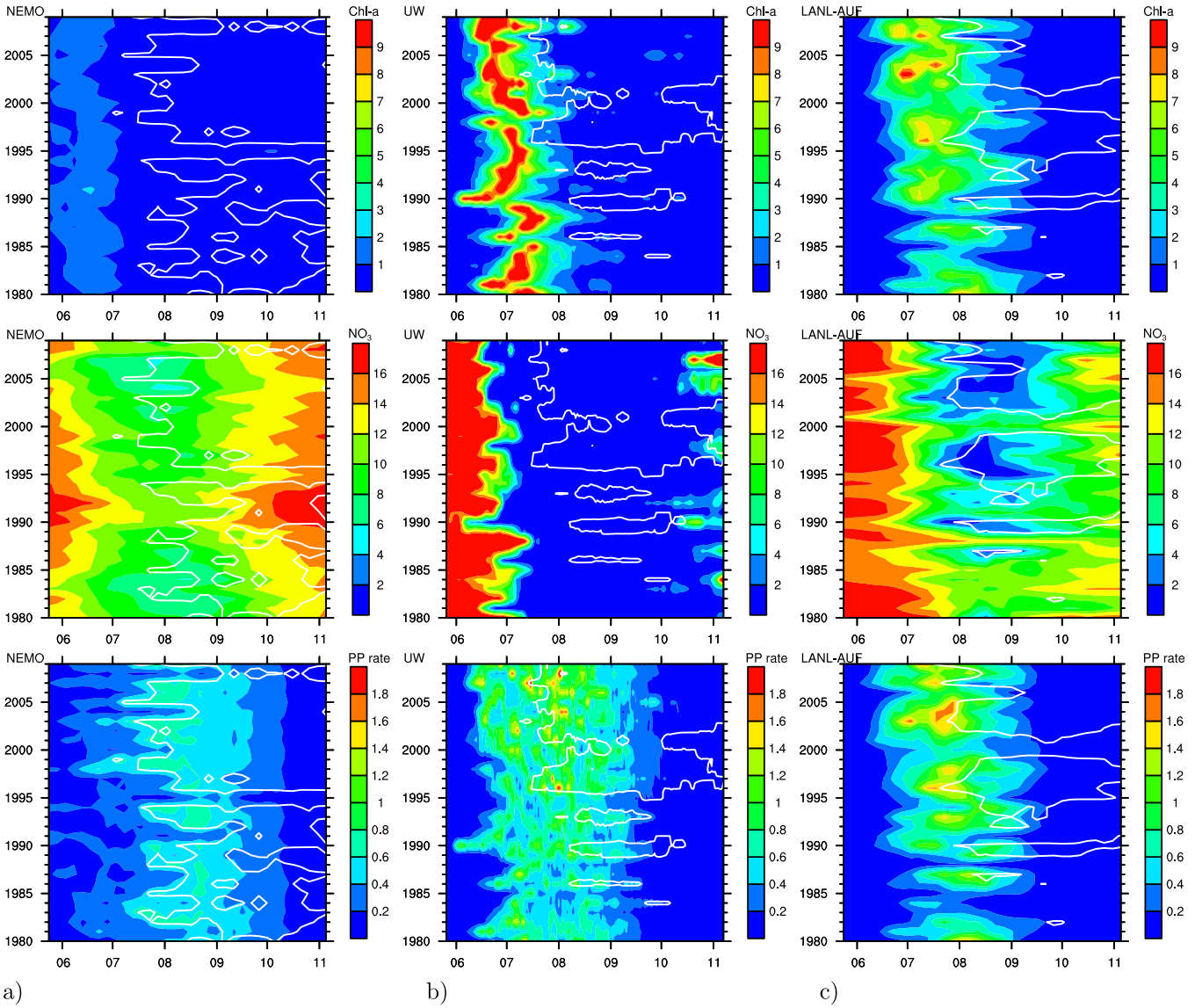

Figure 12. (top row, mg/m^3) Same as Figure 11, except with sea surface Chl-a, (middle row, mmol/m^3) NO_3, and (bottom row, mg C/m^2/d) vertically integrated PP rate.

through assimilation of observational data. Other factors (e.g., snow and ice depth, albedo and light extenuation coefficients) of each sea ice model can also affect the available light in the water column.

Overall, all models concurred that peak timing for under-ice blooming has trended earlier (approximately 10–20 days over the 30 year period), though average timing was different: in mid-June for NEMO, mid-June to early July for UW, and late June to late July for LANL-UAF (Figure 12). The timing of bloom peaks was not necessarily synchronized with the timing of light availability or nutrient consumption across models, suggesting that other factors also contributed significantly to the differences in peak timing at this location, such as advection, vertical mixing, sinking of phytoplankton. Therefore, we should expect a nonuniform response from phytoplankton phenology changes (*Ji et al.,* 2013) to decreasing sea ice cover in different regions of the Arctic Ocean.

4. Discussion and Summary

Although the participating pelagic ecosystem models were originally established based on measurements in open water, the modeled sea surface Chl-a and vertically integrated PP rate under-ice-covered regions were all within the range of observations from 1980 to 2009. Model errors were largest in April, before under-ice bloom begins in the PA and during the early stage of under-ice bloom in the AA. Model results matched the observed

magnitude of Chl-a concentrations and PP rates from mid-May to September, which is the main period for under-ice PP in the Arctic Ocean. The mean model errors of sea surface Chl-a and the vertically integrated PP rate were less than 17% for both PA and AA regions. Agreement between models and observations provided the confidence to analyze long-term changes in under-ice PP versus total PP using model results. The three ecosystem models agreed on the following characteristics and trends for under-ice PP in the Arctic Ocean: (1) under-ice blooms usually begin to grow in mid-April or early May, lasting from May to August, and declining in September; (2) annual average under-ice PP was higher in Arctic Shelf seas than in the Arctic Basin, though ratios of under-ice PP over total PP resembled sea ice concentration, with higher ratios in the basin than in the shelf seas; (3) sea ice changes from 1980 to 2009 were significantly and negatively correlated to changes in total PP and positively related to changes in the ratio for most of the Arctic, but nonsignificantly related to under-ice PP, especially in marginal ice zones; (4) total PP within the Arctic Circle increased at an annual rate of 3.2–8.0 Tg C/yr from 1980 to 2009, due to increases in both areas and PP per unit area in open water. All models showed that the fraction of under-ice PP declined with declining sea ice cover over the last three decades. This change suggests that the Arctic Ocean may be shifting to support a more Subarctic ecosystem in the future, such as that shown in *Grebmeier et al.* [2006] and *Fossheim et al.* [2015]. Changes in light availability in the Arctic Ocean have impacts not only on under-ice PP, but also on benthic communities [*Clark et al.*, 2013] and visual predators [*Varpe et al.*, 2015].

It is encouraging to see models agree on the above large scales and long-term trends of Arctic ecosystem changes. Ecosystem models are sensitive to physical model errors, especially from those processes that affect available light and nutrient transport, such as errors in simulated ice thickness, shortwave radiation, and ocean mixing. A detailed comparison at one location in the Chukchi Sea, where a massive under-ice bloom was observed in 2011 [*Arrigo et al.*, 2012], suggested that all models had simulated the declining sea ice area, earlier arrival of available light, and earlier under-ice bloom, though the magnitude of the light increase differed between models. Under-ice blooms in models with lower light increases had lower Chl-a and were light limited (nutrients were not depleted), while in models with higher light increases, blooms had higher Chl-a and became nutrient limited after the bloom peak. This indicates that ecosystem model simulations of under-ice PP were very sensitive to the light availability computed by atmospheric and sea ice models. PP in the Arctic Basin was expected to increase with decreasing sea ice thickness—e.g., an increased export of sea ice algae [*Boetius et al.*, 2013]. Two of the models indicated such a trend, but another suggested this trend could be nonsignificant in some areas of the deep basin due to nutrient limitation. Given the current low nutrient conditions in the Arctic Basin, future PP changes in the vast Arctic Basin may or may not be correlated to sea ice changes, depending on nutrient availability.

Acknowledgments

We thank P. Matrai (Bigelow Laboratory for Ocean Sciences) for providing data; Y. J. Lee's contribution was supported by NASA NNX13AE81G, awarded to P. Matrai. This work is also supported by the NSF Office of Polar Programs (ARC-0968676, PLR-1417925, PLR-1417677 and PLR-1416920), the NASA Cryosphere (NNX12AB31G) and Climate and Biological Response (NNX11AO91G) programs, and the Research Council of Norway (project 227046 and 244319). The UK authors acknowledge the financial support of the Natural Environmental Research Council (NERC) within the framework of the National Capability and NERC UK Ocean Acidification research (Regional Ocean Modelling project) programs. All authors would like to acknowledge a substantial role played by FAMOS as an excellent forum for the exchange of ideas regarding all aspects of Arctic Ocean modeling and observations. The data used here will be made available upon request (mjin@alaska.edu) after publication.

References

Armstrong, R. A., C. Lee, J. I. Hedges, S. Honjo, and S. G. Wakeham (2002), A new, mechanistic model for organic carbon fluxes in the ocean: Based on the quantitative association of POC with ballast minerals, *Deep Sea Res., Part II*, *49*, 219–236.

Arrigo, K. R., and G. L. van Dijken (2011), Secular trends in Arctic Ocean net primary production, *J. Geophys. Res.*, *116*, C09011, doi:10.1029/2011JC007151.

Arrigo, K. R., et al. (2012), Massive phytoplankton blooms under Arctic sea ice, *Science*, *336*(6087), 1408, doi:10.1126/science.1215065.

Bitz, C. M., and W. H. Lipscomb (1999), An energy-conserving thermodynamic sea ice model for climate study, *J. Geophys. Res.*, *104*, 15,669–15,677, doi:10.1029/1999JC900100.

Boetius, A., et al. (2013), Export of algal biomass from the melting Arctic sea ice, *Science*, *339*(6126), 1430–1432, doi:10.1126/science.1231346.

Clark, G. F., J. S. Stark, E. L. Johnston, J. W. Runcie, P. M. Goldsworthy, B. Raymond, and M. J. Riddle (2013), Light-driven tipping points in polar ecosystems, *Global Change Biol.*, *19*, 3749–3761.

Deal, C. J., M. Jin, S. Elliott, E. Hunke, M. Maltrud, and N. Jeffery (2011), Large-scale modeling of primary production and ice algal biomass within Arctic sea ice in 1992, *J. Geophys. Res.*, *116*, C07004, doi:10.1029/2010JC006409.

Dunne, J. P., J. L. Sarmiento, and A. Gnanadesikan (2007), A synthesis of global particle export from the surface ocean and cycling through the ocean interior and on the seafloor, *Global Biogeochem. Cycles*, *21*, GB4006, doi:10.1029/2006GB002907.

Fossheim, M., R. Primicerio, E. Johannesen, R. B. Ingvaldsen, M. M. Aschan, and A. V. Dolgov (2015), Recent warming leads to a rapid borealization of fish communities in the Arctic, *Nat. Clim. Change*, *5*, 673–677, doi:10.1038/nclimate2647.

Gaspar, P., Y. Grégoris, and J.-M. Lefevre (1990), A simple eddy kinetic energy model for simulations of the oceanic vertical mixing tests at station papa and long-term upper ocean study site, *J. Geophys. Res.*, *95*, 16,179–16,193.

Gill, A. (1982), *Atmosphere-Ocean Dynamics*, *Int. Geophys. Ser.*, vol. 30, Academic Press Inc.

Gradinger, R. (2009), Sea-ice algae: Major contributions to primary production and algal biomass in the Chukchi and Beaufort Seas during May/June 2002, *Deep Sea Res., Part II*, *56*, 1201–1212.

Grebmeier, J. M., J. E. Overland, S. E. Moore, E. V. Farley, E. C. Carmack, L. W. Cooper, K. E. Frey, J. H. Helle, F. A. McLaughlin, and S. L. McNutt (2006), A major ecosystem shift in the Northern Bering Sea, *Science*, *311*(5766), 1461–1464.

Hibler, W. D. (1979), A dynamic thermodynamic sea ice model, *J. Phys. Oceanogr.*, *9*, 815–846.

Hibler, W. D., III (1980), Modeling a variable thickness sea ice cover, *Mon. Weather Rev.*, *108*, 1943–1973.

Hunke, E. C., and J. K. Dukowicz (1997), An elastic-viscous-plastic model for sea ice dynamics, *J. Phys. Oceanogr.*, *27*, 1849–1867.

Hunke, E. C., and M. M. Holland (2007), Global atmospheric forcing data for Arctic ice-ocean modeling, *J. Geophys. Res.*, *112*, C04S14, doi:10.1029/2006JC003640.
Hunke, E. C., W. H. Lipscomb, A. K. Turner, N. Jeffery, and S. Elliott (2013), *CICE: The Los Alamos Sea Ice Model Documentation and Software User's Manual Version 5.0 LA-CC-06-012*, Los Alamos Natl. Lab., Los Alamos, N. M.
Ji, R., M. Jin, O. Varpe (2013), Sea ice phenology and timing of primary production pulses in the Arctic Ocean, *Global Change Biology*, *19*, 734–741, doi:10.1111/gcb.12074.
Jin, M., C. J. Deal, J. Wang, K. H. Shin, N. Tanaka, T. E. Whitledge, S. H. Lee, and R. R. Gradinger (2006), Controls of the landfast ice-ocean ecosystem offshore Barrow, Alaska, *Ann. Glaciol.*, *44*, 63–72.
Jin, M., C. Deal, J. Wang, V. Alexander, R. Gradinger, S. Saitoh, T. Iida, Z. Wan, and P. Stabeno (2007), Ice-associated phytoplankton blooms in the southeastern Bering Sea, *Geophys. Res. Lett.*, *34*, L06612, doi:10.1029/2006GL028849.
Jin, M., C. Deal, S. H. Lee, S. Elliott, E. Hunke, M. Maltrud, and N. Jeffery (2012), Investigation of Arctic sea ice and ocean primary production for the period 1992–2007 using a 3-D global ice-ocean ecosystem model, *Deep Sea Res., Part II*, *81*, 28–35, doi:10.1016/j.dsr2.2011.06.003.
Jones, C. D., et al. (2011), The HadGEM2-ES implementation of CMIP5 centennial simulations, *Geosci. Model Dev.*, *4*, 543–570, doi:10.5194/gmd-4-543-2011.
Kishi, M. J., et al. (2007), NEMURO—A lower trophic level model for the North Pacific marine ecosystem, *Ecol. Modell.*, *202*, 12–25.
Klaas, C., and D. Archer (2002), Association of sinking organic matter with various types of mineral ballast in the deep sea: Implications for the rain ratio, *Global Biogeochem. Cycles*, *16*(4), 1116, doi:10.1029/2001GB001765.
Kwiatkowski, L., et al. (2014), iMarNet: An ocean biogeochemistry model intercomparison project within a common physical ocean modelling framework, *Biogeosciences*, *11*, 7291–7304, doi:10.5194/bg-11-7291-2014.
Large, W. G., and S. G. Yeager (2009), The global climatology of an interannually varying air sea flux data set, *Clim. Dyn.*, *33*, 341–364, doi:10.1007/s00382-008-0441-3.
Large, W. G., J. C. McWilliams, and S. C. Doney (1994), Oceanic vertical mixing: A review and a model with a vertical K-profile boundary layer parameterization, *Rev. Geophys.*, *32*, 363–403.
Lindsay, R. W., and J. Zhang (2006), Assimilation of ice concentration in an ice-ocean model, *J. Atmos. Oceanic Technol.*, *23*, 742–749.
Lipscomb, W. H., and E. C. Hunke (2004), Modeling sea ice transport using incremental remapping, *Mon. Weather Rev.*, *132*, 1341–1354.
Madec, G. (2008), NEMO Reference Manual, Ocean Dynamic Component: NEMO-OPA, Note du Pole de modélisation, *Tech. Rep. 27*, Note du Pole de Modélisation, Inst. Pierre Simmon Laplace, Paris, ISSN: 1288-1619.
Madec, G., P. Delecluse, M. Imbard, and C. Lévy (1998), OPA 8.1 Ocean General Circulation Model Reference Manual, *Tech. Rep. 11*, 91 pp., Note du Pole de Modélisation, Inst. Pierre Simon Laplace, Paris.
Manda, A., N. Hirose, and T. Yanagi (2005), Feasible method for the assimilation of satellite-derived SST with an ocean circulation model, *J. Atmos. Oceanic Technol.*, *22*(6), 746–756, doi:10.1175/JTECH1744.1.
Marchuk, G. I., and B. A. Kagan (1989), *Dynamics of Ocean Tides*, 327 pp., Kluwer Acad., Norwell, Mass.
Matrai, P. A., E. Olson, S. Suttles, V. Hill, L. A. Codispoti, B. Light, and M. Steele (2013), Synthesis of primary production in the Arctic Ocean. I: Surface waters, 1954–2007, *Prog. Oceanogr.*, *110*, 93–106.
Mongin, M., D. M. Nelson, P. Pondaven, and P. Tréguer (2006), Simulation of upper-ocean biogeochemistry with a flexible-composition phytoplankton model: C, N and Si cycling and Fe limitation in the Southern Ocean, *Deep Sea Res., Part II*, *53*, 601–619.
Moore, J. K., S. C. Doney, J. C. Kleypas, D. M. Glover, and I. Y. Fung (2002), An intermediate complexity marine ecosystem model for the global domain, *Deep Sea Res., Part II*, *49*, 403–462.
Moore J. K., S. C. Doney, and K. Lindsay (2004), Upper ocean ecosystem dynamics and iron cycling in a global three-dimensional model, *Global Biogeochem. Cycles*, *18*, GB4028, doi:10.1029/2004GB002220.
Pabi, S., G. V. Dijken, and K. R. Arrigo (2008), Primary production in the Arctic Ocean 1998–2006, *J. Geophys. Res.*, *113*, C08005, 10.1029/2007JC004578.
Popova, E. E., A. Yool, A. C. Coward, F. Dupont, C. Deal, S. Elliott, E. Hunke, M. Jin, M. Steele, and J. Zhang (2012), What controls primary production in the Arctic Ocean? Results from an intercomparison of five general circulation models with biogeochemistry, *J. Geophys. Res.*, *117*, C00D12, doi:10.1029/2011JC007112.
Popova, E. E., A. Yool, Y. Aksenov, A. C. Coward, and T. R. Anderson (2014), Regional variability of acidification in the Arctic: A sea of contrasts, *Biogeosciences*, *11*, 293–308, doi:10.5194/bg-11-293-2014.
Ridgwell, A., I. Zondervan, J. C. Hargreaves, J. Bijma, and T. M. Lenton (2007), Assessing the potential long-term increase of oceanic fossil fuel CO_2 uptake due to CO_2-calcification feedback, *Biogeosciences*, *4*, 481–492, doi:10.5194/bg-4-481-2007.
Röske, F. (2001), An atlas of surface fluxes based on the ECMWF reanalysis—A climatological data set to force global ocean general circulation models, *Tech. Rep. 323*, Max-Planck-Inst. fur Meteorol., Hamburg, Germany.
Schweiger, A., R. W. Lindsay, J. Zhang, M. Steele, H. Stern, and R. Kwok (2011), Uncertainty in modeled Arctic sea ice volume, *J. Geophys. Res.*, *116*, C00D06, doi:10.1029/2011JC007084.
Semtner, A. J. (1976), A model for the thermodynamic growth of sea ice in numerical investigation of climate, *J. Phys. Oceanogr.*, *6*, 376–389.
Smith, R., and P. Gent (2002), Reference manual for the Parallel Ocean Program (POP), *Tech. Rep. LAUR-02-2484*, Los Alamos Natl. Lab., Los Alamos, N. M.
Smith, R., and P. R. Gent (2004), Anisotropic Gent-McWilliams parameterization for ocean models, *J. Phys. Oceanogr.*, *34*, 2541–2564, doi:10.1175/JPO2613.1.
Smith, R. D., J. K. Dukowicz, and R. C. Malone (1992), Parallel ocean general circulation modeling, *Physica D*, *60*, 38–61.
Timmermann, R., H. Goosse, G. Madec, T. Fichefet, C. Ethe, and V. Duliere (2005), On the representation of high latitude processes in the ORCA-LIM global coupled sea ice-ocean model, *Ocean Modell.*, *8*, 175–201, doi:10.1016/j.ocemod.2003.12.009.
Varpe, Ø., M. Daase, and T. Kristiansen (2015), A fish-eye view on the new Arctic lightscape, *ICES J. Mar. Sci.*, *72*, 2532–2538, doi:10.1093/icesjms/fsv129.
Yool, A., E. E. Popova, and T. R. Anderson (2013a), MEDUSA-2.0: An intermediate complexity biogeochemical model of the marine carbon cycle for climate change and ocean acidification studies, *Geosci. Model Dev. Discuss.*, *6*, 1259–1365, doi:10.5194/gmdd-6-1259-2013.
Yool, A., E. E. Popova, A. C. Coward, D. Bernie, and T. R. Anderson (2013b), Climate change and ocean acidification impacts on lower trophic levels and the export of organic carbon to the deep ocean, *Biogeosciences*, *10*, 5831–5854, doi:10.5194/bg-10-5831-2013.
Zhang, J., and D. A. Rothrock (2003), Modeling global sea ice with a thickness and enthalpy distribution model in generalized curvilinear coordinates, *Mon. Weather Rev.*, *131*(5), 681–697.
Zhang, J., and M. Steele (2007), The effect of vertical mixing on the Atlantic water layer circulation in the Arctic Ocean, *J. Geophys. Res.*, *112*, C04S04, doi:10.1029/2006JC003732.

Zhang, J., Y. H. Spitz, M. Steele, C. Ashjian, R. Campbell, L. Berline, and P. Matrai (2010a), Modeling the impact of declining sea ice on the Arctic marine planktonic ecosystem, *J. Geophys. Res.*, *115*, C10015, doi:10.1029/2009JC005387.

Zhang, J., R. Woodgate, and R. Moritz (2010b), Sea ice response to atmospheric and oceanic forcing in the Bering Sea, *J. Phys. Oceanogr.*, *40*, 1729–1747, doi:10.1175/2010JPO4323.1.

Zhang, J., C. Ashjian, R. Campbell, V. Hill, Y. H. Spitz, and M. Steele (2014), The great 2012 Arctic Ocean summer cyclone enhanced biological productivity on the shelves, *J. Geophys. Res. Oceans*, *119*, 297–312, doi:10.1002/2013JC009301.

Zhang, J., C. Ashjian, R. Campbell, Y. H. Spitz, M. Steele, and V. Hill (2015), The influence of sea ice and snow cover and nutrient availability on the formation of massive under-ice phytoplankton blooms in the Chukchi Sea, *Deep Sea Res., Part II*, *118*, 122–135, doi:10.1016/j.dsr2.2015.02.008.